

ORIGINAL ARTICLE

A Machine-Learning-Based Approach to Solve Both Contact Location and Force in Soft Material Tactile Sensors

Luca Massari^{1,2,3}, Emiliano Schena⁴, Carlo Massaroni⁴, Paola Saccomandi⁵, Arianna Menciassi^{1,2}, Edoardo Sinibaldi^{6,*}, and Calogero Maria Oddo^{1,2,*}

Abstract

This study addresses a design and calibration methodology based on numerical finite element method (FEM) modeling for the development of a soft tactile sensor able to simultaneously solve the magnitude and the application location of a normal load exerted onto its surface. The sensor entails the integration of a Bragg grating fiber optic sensor in a Dragon Skin 10 polymer brick (110 mm length, 24 mm width). The soft polymer mediates the transmission of the applied load to the buried fiber Bragg gratings (FBGs), and we also investigated the effect of sensor thickness on receptive field and sensitivity, both with the developed model and experimentally. Force-controlled indentations of the sensor (up to 2.5 N) were carried out through a cylindrical probe applied along the direction of the optical fiber (over an ~90 mm span in length). A finite element model of the sensor was built and experimentally validated for 1 and 6 mm thicknesses of the soft polymeric encapsulation material, considering that the latter thickness resulted from numerical simulations as leading to optimal cross talk and sensitivity, given the chosen soft material. The FEM model was also used to train a neural network so as to obtain the inverse sensor function. Using four FBG transducers embedded in the 6-mm-thick soft polymer, the proposed machine learning approach managed to accurately detect both load magnitude ($R = 0.97$) and location ($R = 0.99$) over the whole experimental range. The proposed system could be used for developing tactile sensors that can be effectively used for a broad range of applications.

Keywords: soft tactile sensor, fiber Bragg grating, contact force sensing, contact position localization, FEM-based machine learning

¹ The BioRobotics Institute, Scuola Superiore Sant'Anna, Pisa, Italy.

² Department of Excellence in Robotics & AI, Scuola Superiore Sant'Anna, Pisa, Italy.

³ Department of Linguistics and Comparative Cultural Studies, Ca' Foscari University of Venice, Ca' Bembo, Venezia, Italy.

⁴ Research Unit of Measurements and Biomedical Instrumentation, Center for Integrated Research, Università Campus Bio-Medico di Roma, Roma, Italy.

⁵Department of Mechanical Engineering, Politecnico di Milano, Milano, Italy.

⁶Center for Micro-BioRobotics, Istituto Italiano di Tecnologia, Pontedera, Italy.

* These two authors share equal contribution and supervision to this work.

Introduction

TACTILE SENSING ALLOWS DETERMINING, BY MEANS OF CONTACT, OBJECTS' PHYSICAL PROPERTIES. TOUCH PLAYS A KEY ROLE IN HUMAN INTERACTION with the surrounding environment by encoding information about properties such as temperature, pain, force, pressure, texture, and shape detection. Information arises from the multiple receptors available within the human skin, in particular in hands and fingers.^{1,2} Moreover, tactile sensing supports most of the manipulation tasks such as object handling, grasping, controlling, and many other associated tasks.³

Artificial tactile sensors should be able to measure contact conditions such as force and location and to retrieve related geometrical information. The fields of application of tactile sensing include prosthetics,^{4–6} medicine,⁷ dentistry,⁸ minimally invasive surgery,⁹ augmented and virtual reality,^{10,11} telepresence,^{12,13} mechatronics,¹⁴ and robotics.^{15–17} Providing a tactile feedback is essential to perform manipulation tasks autonomously or to retrieve interaction information.^{18–20}

Conventional tactile sensors are usually built using inflexible and relatively stiff materials that limit their capacity to deform or to adapt their shapes to external constraints. Regardless of their high resolution or precision, such sensors tend to be functional only in a specific domain. The emerging class of soft materials, which include deformable components such as gels, polymers, and fluids, represents a solution for the increasing demand of flexibility.^{21–24} Nowadays, state of the art provides evidence of the development of soft tactile sensors used in several applications.^{25–30} Next, soft tactile sensor generations will be able to change configuration depending on the surface where they are integrated. Along with this trend, in this article, we adopt a soft material to realize a flexible tactile sensor. The tactile transducer has to be flexible as well, so to be integrated into the soft matrix. Among all the available technologies, optical fibers can successfully meet the aforementioned requirements. The use of optical fibers as sensing elements in tactile sensors is growing fast thanks to their characteristics such as flexibility, electromagnetic immunity, high sensitivity, light weight, multiplexing, and distributed sensor capabilities.^{31–34} Such sensors can be considered a good alternative to traditional sensors to measure mechanical variables. Indeed, optical fibers are used with promising results in different scenarios, such as smart textiles,³⁵ automotive,³⁶ medicine,³⁷ and civil engineering.³⁸ Fiber optic-based sensors can be developed in different ways depending on the adopted working principle, for example, hybrid optoelectronic,³⁹ micro- and macrobending,^{40,41} interferometry,⁴² and fiber Bragg grating (FBG) sensors.^{43–45} The latter technology was chosen for our soft sensor, due to its reliability in measuring strain and capability to use a single fiber for reading information from multiple transducers, via wavelength separation.^{46–52} State of the art on FBG technology gives evidence of different scenarios. Typically, such gratings are used as elongation sensors leveraging the axial deformation of the gratings, with illustrative applications, including cardiac and respiratory monitoring,⁵³ structural monitoring of bridges,⁵⁴ and tissue palpation in minimally invasive surgery.⁴⁴ Moreover, FBGs have been successfully used also for the development of tactile sensors.⁵⁵ In this article, we present a soft tactile sensor based on FBG sensing elements that, compared with related works,^{45–48,50} shares the idea of embedding the optical fiber inside a soft polymer that mediates loads applied to the buried FBGs. Among the

available soft materials, we chose the Dragon Skin 10 medium (Smooth-on, USA) due to its low delamination and high flexibility, and we investigated its behavior with the developed finite element method (FEM) numerical model. Within this article, we intend to measure the force and, simultaneously, to locate the point of contact between the sensor and the objects. Accurate detection of both variables is crucial for many applications and it is still an open research topic. We defined the force range (up to 2.5 N) by considering gentle touch tasks such as those typically occurring in fine manipulation activities.^{13,56–60} Moreover, we advance the state of the art by proposing a model-based calibration to obtain the sensor inverse function using machine learning. A neural network for force coding of a tactile sensor based on FBG was proposed by Saccomandi *et al.*,⁴⁵ whereas, differently from this work, the training set was retrieved exclusively from experimental data and there was no indentation localization. Provided that the model is accurate, this approach can significantly reduce individual calibration requirements of soft tactile sensors and the time to market, enhancing their industrial impact. In the present study, a FEM simulation of the sensor has been used to generate a huge set of data to train a neural network, later validated through experimental data, and thus getting the inverse function from the sensor output, namely the load amplitude and position. Moreover, the numerical model has been used to study the influence of design parameters (i.e., thickness of the soft encapsulating material) on the FBG response, in searching the optimal trade-off between sensitivity and receptive field. Our investigation on the effect of thickness complements the study recently published by Lun *et al.*,⁶¹ focused on shape sensing. The present work is organized as follows: in the Materials and Methods section, we present the sensor design followed by the numerical model and the adopted constraints. Then, a brief description of the FBG working principle and its application to our sensor is given. Both numerical and experimental results are presented in the Results section: model simulation, experimental data, comparison between model and experimental data and neural network results. Finally, discussion and concluding remarks are reported in the last section.

Materials and Methods

Development of the soft sensor integrating FBG transducers

The sensor was fabricated by embedding an optical fiber throughout a soft polymeric matrix to obtain a thin and flexible pad, leading to sensors that could be easily wrapped, embedded, or attached to a specific surface.

FBGs are microstructures with a typical length between 1 and 15 mm inscribed in the core of a single-mode optical fiber. The realization process is based on the transverse illumination of the fiber with an ultraviolet laser beam and the generation of an interference pattern in its core through a phase mask. Therefore, a resonant structure is created by means of a spatial periodic modulation of the refraction core index. When a light source is injected into the optical fiber, generally with an optical interrogator, the FBG acts as a narrow band filter: part of the light is transmitted and goes through the fiber, while another narrow part is reflected back. Such a reflected spectral segment is centered around the Bragg wavelength (λ_B) and it is defined by the effective refraction index (n_{eff}) of the fiber core and the grating period (Λ_B) as in Equation (1):

$$\lambda_B = 2 \eta_{eff} \Lambda_B \quad (1)$$

FBGs are sensitive to strain that leads to variations of λ_B .

One of the main advantages of FBGs is the possibility to add multiple gratings in a single optical fiber, provided that a constraint is respected: all the reflected wavelengths need to be different, thus avoiding overlapping and consequentially data loss from one or more FBGs. The chosen optical

fiber (DTG's In Reduced Cladding Fibers; FBGS, Geel, Belgium), 115 μm of diameter, housed four FBGs placed along its length in selected slots. The length of each grating was 8 mm; the center to center distance between adjacent FBGs was 12 mm (d) between FBG1-FBG2 and FBG3-FBG4, and 48 mm ($3d$) between FBG2 and FBG3 (Fig. 1A). FBG1 and FBG2 were placed at a distance d to evaluate the cross talk between close adjacent gratings. Then, a distance $3d$ was set between FGB2 and FBG3 so to evaluate the relationship between material thickness and sensor positioning with respect to combined force position measurement accuracy. Furthermore, the fourth grating (FBG4) was added for obtaining a symmetric configuration (FBG1-FBG2 vs. FBG3-FBG4) that was also functional for investigating reproducibility in a single setup. The following nominal reflected wavelengths were chosen for the FBGs in the proposed sensor: 1544, 1546, 1553, and 1555 nm (from FBG1 to FBG4). The polymer used to cover the sensor was Dragon Skin (10 medium; Smooth-on). This silicone rubber is highly stretchable (high elongation at break)⁶² and soft (shore A 10), thus enabling the sensor to be twisted, wrapped, bent, and stretched (Fig. 1C; Supplementary Video S1). Moreover, such a rubber allows for a proper demolding of the sensor, without delamination of the thin polymer layer.

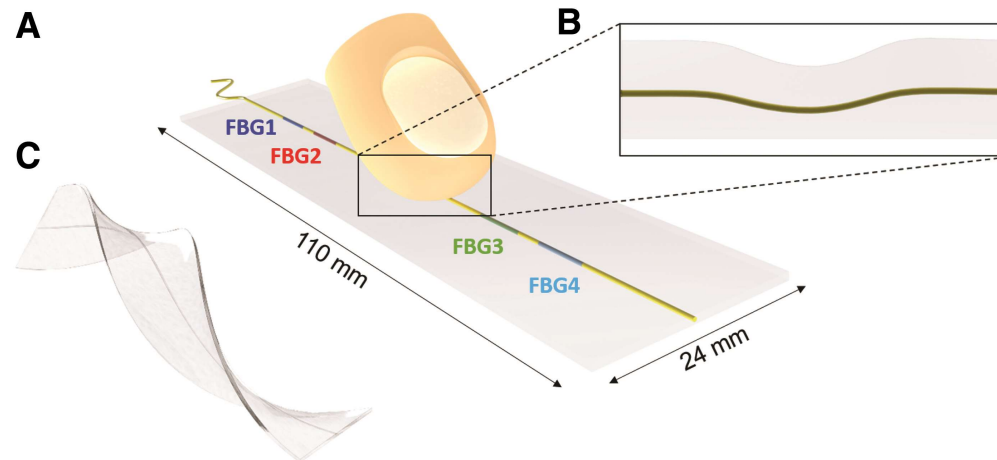


FIG. 1. (A) Ultrasoft tactile sensor array integrating FBG transducers (marked in colors). (B) Inset of the sensor highlighting the effect of the applied load on it. (C) Deformability and ultrasoft properties of the sensor. FBG, fiber Bragg grating. Color images are available online.

The sensors had a parallelepiped shape and same physical dimension apart from the thickness (thickness refers to the whole encapsulating material, with the optical fiber embedded at the middle of the brick). They were 110 mm long, 24 mm wide, and with a variable thickness, ranging from 1 to 8 mm in the performed FEM simulations. Following the simulations, two sensors were fabricated, with 1 and 6 mm thickness, respectively. The optical fiber was aligned with the longitudinal axis and laterally centered in the middle of the brick. During the fabrication process, the liquid polymer was cast inside a customized mold. To minimize air bubbles, vacuum degassing of the liquid rubber was performed before casting. The optical fiber was held in the desired position in the mold before starting the casting process. The rubber was cured at room temperature until solidification and subsequent demolding of the sensor.

As shown in Figure 1A, we applied loads along the sensor top surface. The polymeric matrix mediated the transmission of the applied load to the optical fiber, thus passing from an unstrained to a strained condition, as highlighted in the inset (Fig. 1B). Figure 2 explains the FBG working principle applied to our study. In the upper part of the figure, a lateral view of the sensor is presented, illustrating six example cases, from no indentation (N) to indentation in five locations (P1–P5). In the bottom part of Figure 2, the outputs of two FBGs are displayed for both 1-mm-thick and 6-mm-thick sensors. Each case refers to a particular indentation site, apart from N , which represents the null load condition (unstrained condition for the optical fiber). P2 and P4 correspond to the cases where the load is applied above FBG1 (for P2) and FBG2 (for P4). Such conditions represent, respectively, the cases with maximum strain suffered by FBG1 and FBG2 and thus with maximum shift of the reflected signals; indeed, higher strain entails higher grating period variation and thus higher shifts of the reflected wavelengths. The influence of the thickness of the soft polymeric packaging material on the strain acting on the optical fiber is investigated in the present study.

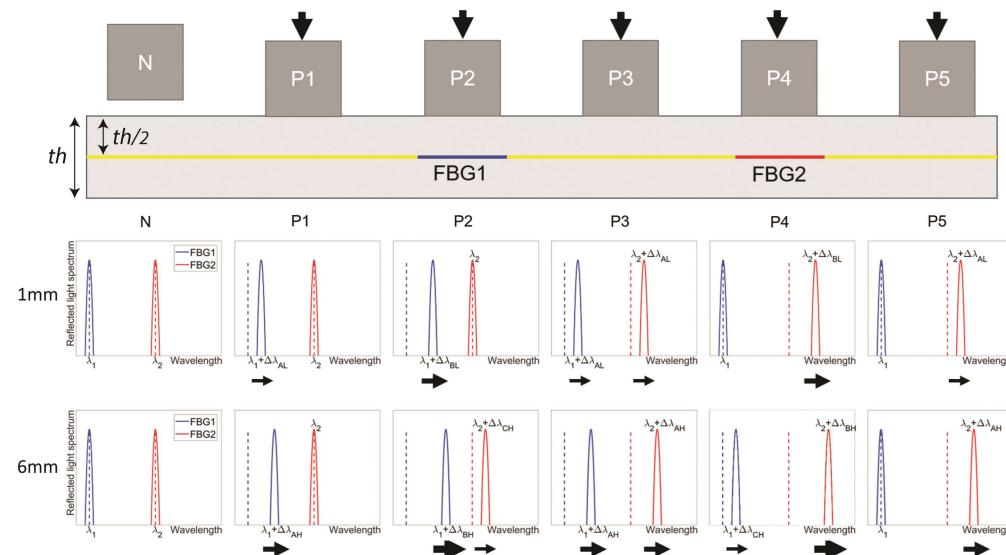


FIG. 2. Working principle of the FBG transducers in the developed phantom. Only FBG1 and FBG2 are shown for ease of illustration. Color images are available online.

Soft sensor FEM simulation

A FEM simulation of the sensors was performed by means of COMSOL Multiphysics (COMSOL, Inc., Palo Alto, CA), with the structural mechanics module. Such simulations addressed the evaluation of load/unload cycles applied onto the sensor surface. Moreover, we investigated the effect of thickness in determining a suitable trade-off between receptive field and sensitivity. The developed model was used to generate a very large data set to train a neural network to obtain the sensor inverse function, namely the detection of the indentation sites and the applied load. The model reproduced the sensor with parametric thickness, in the 1 to 8 mm range. We assumed to deal with linear elastic sensor deformations (working assumption). Hence, we defined the Young's modulus (E), Poisson coefficient (ν), and density (d) for both the encapsulation polymer and the optical fiber. The following values were retrieved for the rubber in pertinent literature^{63–67}: $E = 100 \text{ kPa}$, $\nu = 0.49$, $d = 1070 \text{ kg/m}^3$, while for the optical fiber

we adopted the values reported in the datasheet, that is, $E = 36$ GPa, $\nu = 0.17$, $d = 2203$ kg/m³. The simulation was based on the experimental protocol described in the following section, which consisted in applying a load onto a specific location of the sensor through a cylindrical indenter. The load was applied on an area equal to the size of the cylindrical indenter surface along the sensor top side. Each pair of force and position values corresponded to a certain strain of the fiber. In this work, the used force ranged between 0.1 and 2.5 N, with steps of 0.1 N, and the indentation position between 0 and 86 mm, with steps of 0.25 mm. Since the sensor was attached to a flat rigid surface, in the FEM simulation, a null displacement was set at the bottom surface of the sensor. We assumed a perfect bonding between the optical fiber and the encapsulation polymer. We adopted some simplifications in the model with the aim to reduce the computational time needed to retrieve the solution. Taking into account the small diameter of the optical fiber, Ø 115 µm, with respect to the thickness of the sensor (1 or 6 mm), we described the optical fiber by means of a truss element, that is, a slender member that can only sustain axial forces. Such a modification allowed to treat the optical fiber as a 1D solid. Moreover, thanks to the symmetry of the sensor, we only considered half sensor, thus further reducing the computational burden. Mesh independence was carefully obtained through preliminary runs. In particular, we applied a finer mesh around the optical fiber and on the surface where we applied the normal load (i.e., indenter area).

Experimental setup and protocol

The experimental phase was carried out by means of a mechatronic platform, developed to perform automatic force-controlled indentation throughout the sensor surface (Fig. 3). Motorized translational stages ensured the motion of the sensor along the Cartesian axes. Such stages allowed motion with a 2.5 µm step resolution along the horizontal axis (8MTF-102LS05; STANDA, Vilnius, Lithuania) and motion with a 5 µm step resolution along the vertical axis (8MVT120-25-4247). An aluminum cylindrical probe of 6 mm diameter was used to indent the sample. We conservatively chose the indenter diameter to be smaller than the characteristic minimum size (1 cm) of objects manipulated in precision grasping task of daily life.⁶⁸ A load cell (Nano 43; ATI Industrial Automation, Apex, NC), mechanically linked to the indenter, was used to collect data about the force arising from the contact between sensor and probe. Moreover, such a load cell was responsible for the trigger generated upon reaching the threshold value (F_{max}) used to pilot the indentations. An optical interrogator (si425; Micron Optics, Atlanta, GA) was used to collect the data coming out from the FBG transducers, namely the reflected wavelengths of the different gratings. All the components of the setup were controlled through LabVIEW routines (National Instruments Corp., Austin, TX) by means of a PC graphical user interface (Fig. 3E). The software ensured the synchronization of the data coming out from the load cell and the optical interrogator, thus enabling and facilitating data elaboration (Supplementary Fig. S1).

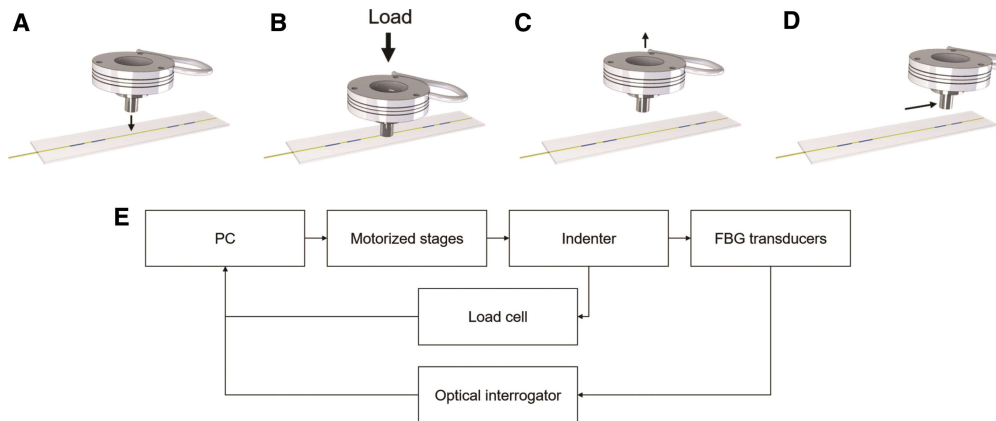


FIG. 3. (A–D) Indentation process during the experimental acquisition (the direction of the arrow indicates relative motion). **(E)** Block diagram of the experimental setup. Color images are available online.

The protocol consisted of automatic force-controlled indentations of the sensor in different sites and using several F_{\max} (i.e., load/unload cycles). We considered as reference position a point located 12 mm before the center of the first grating (FBG1). The X coordinates of the indentations ranged from this reference position up to 86 mm with 2 mm steps. The F_{\max} ranged from 1 N up to 2.5 N with steps of 0.5 N (i.e., on each site 4 indentations were performed). Considering such a procedure, we obtained 176 load/unload indentations (44 sites and 4 forces) that were repeated 3 times each.

FEM-based machine learning to retrieve sensor inverse function and experimental data analysis

As a first step, we assessed the predictive capability of the numerical model that was used to train a neural network so as to obtain the inverse sensor function. During the experimental sessions, indentation force values, indentation sites, and FBG reflected wavelengths were stored. Each indentation we retrieved the maximum normal force value, the position of the indenter, and the corresponding reflected wavelength of the four FBGs. Such values were then compared with the numerical model output to validate the proposed simulations. The strain experienced by the fiber during the load/unload cycle of the cylindrical indenter was retrieved from the FEM simulations. Moreover, the solid displacement of the soft polymer and the coupled relative displacement of the optical fiber were analyzed.

Each pair of probe position and exerted force corresponded to a certain axial strain of the fiber. Since the position of the four FBG transducers along the fiber, the F_{\max} level, and the indentation sites were known experimental parameters, we used the strain (ε) retrieved from the numerical model to build the sensor direct function and, thus, to obtain the reflected wavelengths.

The strain was converted into reflected wavelengths via Equation (2).

$$\Delta\lambda_B = 0.78 \cdot \lambda_B \cdot \varepsilon, \quad (2)$$

where λ_B is the reflected wavelength and ε is the strain suffered by the fiber. To obtain the sensor inverse function using machine learning, we designed a cascade of two feedforward neural networks, each one with 10 hidden neurons. More specifically, the architecture of each neural network was a two-layer feedforward network with sigmoid hidden neurons and output neurons. The Levenberg–Marquardt method was used to train the

network. The first neural network (NN1) had four inputs, which were the FBG reflected wavelengths, and one output, which was the estimated position. The second neural network (NN2) was in cascade, with five inputs, which were the four FBG reflected wavelengths plus the position estimated by NN1, and one output, which was the estimation of the applied force (Fig. 4B). For the cascade of both neural networks (NN1 and NN2), we used the FEM model data as training set, part of the experimental data (25% of the total) as validation set, and the rest of the experimental data (75% of the total) as test set. FEM model data were used to train both the neural networks, using the Levenberg–Marquardt training algorithm. The performance of the neural network was assessed by mean of root mean square error (RMSE) and correlation coefficient (R) between output and target.

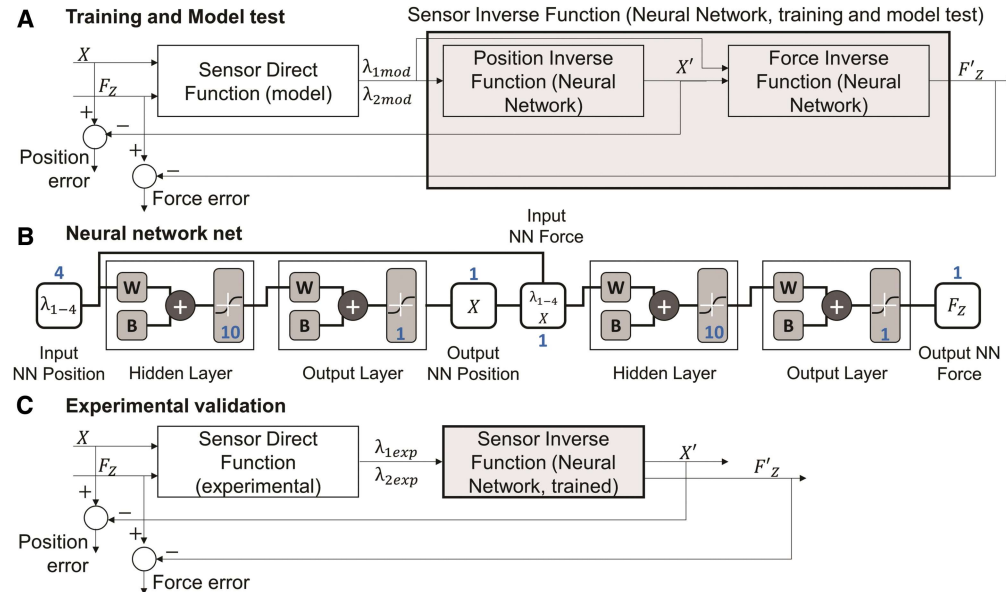


FIG. 4. Machine-learning-based construction of the sensor inverse function. **(A)** Block diagram of the training part based on the numerical model. **(B)** Graphical view of the network connectivity. **(C)** Block diagram of the validation part based on the experimental data. NN, neural network. Color images are available online.

We applied the same procedure to the experimental data as well (Fig. 4B), thus first retrieving the reflected wavelengths from the sensor direct function (experimental) and then obtaining the sensor inverse function using the trained neural network. Experimental data were also used to validate the neural networks. The whole data processing was performed by means of the Neural Networks toolbox (MATLAB; The MathWorks, Inc., Natick, MA).

Results

FEM model results

Numerical model results are summarized (Fig. 5). Figure 5D shows the model of the 1-mm-thick sensor, with an overall view of the fiber strain. Figure 5E represents the axial strain suffered by the optical fiber as a function of the distance from the indenter. Figure 5A–C and F–H shows the behavior of the encapsulating polymer and the optical fiber, respectively. The chosen graphs are 2D cut-views on the sagittal plane through the fiber and the indenter axis, and they highlight the solid displacement due to the applied load (on the left for the polymeric matrix, and on the right for the optical fiber). For a given load, changes in the sensor thickness lead to a change in the axial strain transduced by the optical fiber, affecting the receptive field. We thus numerically investigated the effect of sensor thickness on the axial strain, which is shown in Figure 6. Counterintuitively, by increasing the thickness, the axial strain propagating in the soft material up to the FBG sites increases as well in an initial range of thickness. For thickness above 6 mm, the trend reverts and the axial strain starts decreasing.

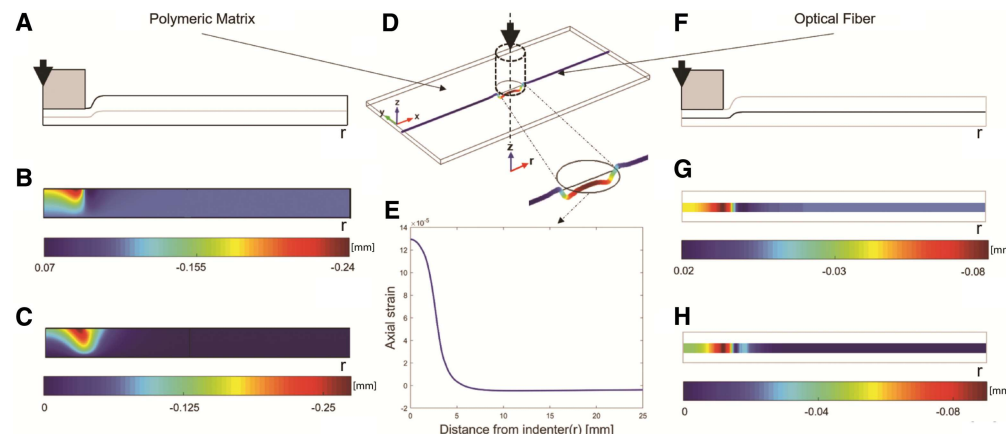


FIG. 5. (A) Schematic of the solid displacement due to the applied load (half sensor is considered in the *whole panel*, thanks to symmetry). (B) Contour plot of the z displacement of the polymeric matrix versus the radial distance (r) from the indenter axis. (C) Contour plot of the displacement of the polymeric matrix. (D) 3D view also showing the axial strain experienced by the optical fiber during indentation. (E) Graph showing the axial strain versus the radial distance (r). (F–H) Same for the panel (A–C), but not for the optical fiber. Color images are available online.

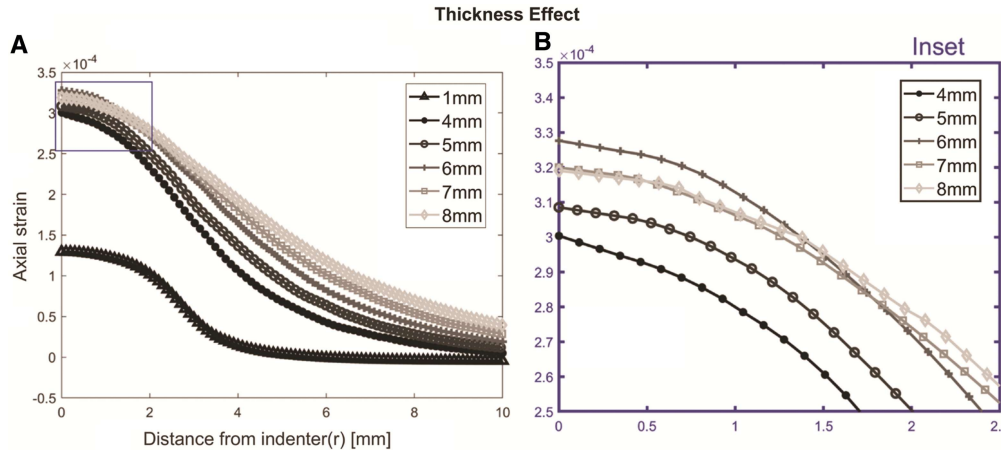


FIG. 6. (A) Axial strain of the optical fiber for different thicknesses of the sensor. (B) Detail of the panel A highlighting the axial strain under the indenter. As shown in Figure 2, the thickness refers to the whole encapsulating material, with the optical fiber embedded at the *middle of the brick*. Color images are available online.

Experimental results

Figure 7 shows the reflected wavelengths for the four FBGs as a function of the indentation location both for the experimented force values and normalized with respect to force, highlighting a linear response in the considered range of forces. This result highlights the difference in receptive field between the 1-mm-thick sensor (dashed lines) and the 6-mm-thick sensor (straight lines); counterintuitively, for the same load and indentation site, higher thickness values permit to enhance strain transmission. Cross talk between adjacent FBGs is a key factor since it allows the joint discrimination of force and position by means of the neural network. The output of the thinner sensor has no cross talk between FBG2 and FBG3 and nearly negligible cross talk between FBG1 and FBG2 or between FBG3 and FBG4, whereas the thicker sensor shows a considerable cross talk in both cases. Moreover, Figure 7D shows the relationship between the sensor output (i.e., wavelength variation) and the applied load for indentations performed with different forces onto the center of each of the gratings. Figure 7D demonstrates linearity ($R^2 = 0.995$ for 6 mm thickness and $R^2 = 0.983$ for 1 mm thickness) and repeatability (maximum 0.08 nm standard and mean 0.018 nm standard of $\Delta\lambda$ over the force range for 6 mm thickness and maximum 0.03 nm standard and mean 0.007 nm standard of $\Delta\lambda$ over the force range for 1 mm thickness), as well as greater sensitivity of the thicker sensor.

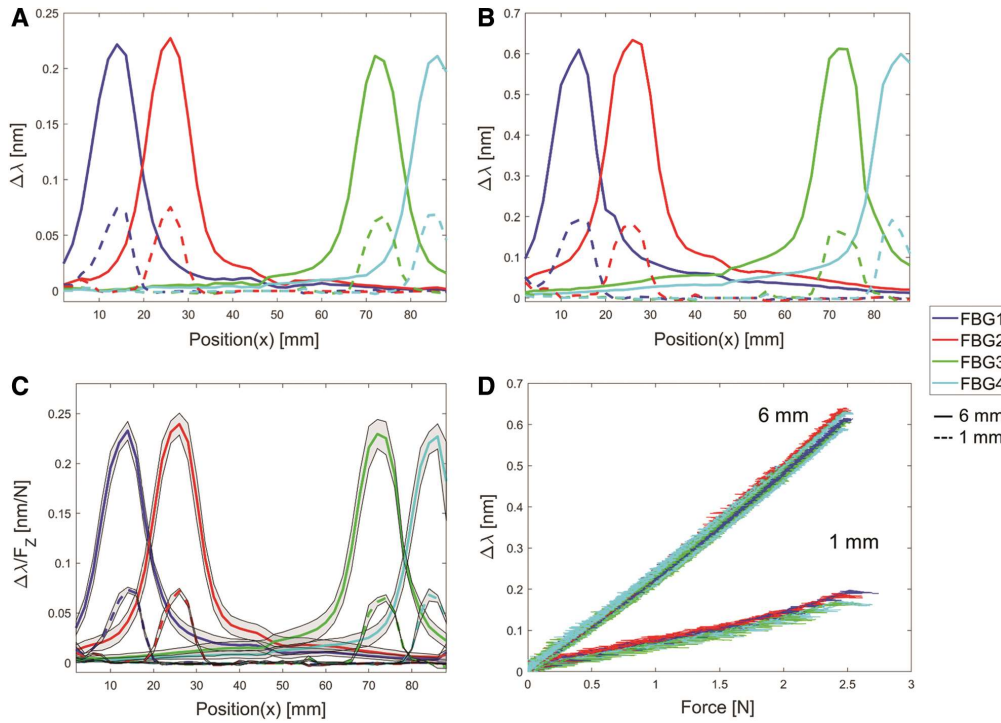


FIG. 7. Experimental data showing the wavelength variation of the different FBG sensors as a function of the position of the applied load for both the sensors 1 mm (*dashed lines*) and 6 mm (*continuous lines*). **(A)** The wavelength shift function of the position is represented for 1 N indentation force. **(B)** The wavelength shift function of the position is represented for 2.5 N indentation force. **(C)** The wavelength shift per unit indentation force is represented to highlight the linear character observed for the corresponding trend (some deviations being associated with higher indentation forces). **(D)** Relationship between the sensor output (wavelength variation) and the applied load for indentations performed with different forces onto the center of each of the gratings. For each thickness (1 mm *dotted line* and 6 mm *solid line*), the plots show 48 data sets: the transient forces spanned, while targeting 4 force values (1 N, 1.5 N, 2 N, 2.5 N), for 4 FBG transducers and 3 experimental repetitions. Color images are available online.

Model validation

The comparison between numerical simulations and experimental data is shown in Figure 8 (1-mm-thick sensor on the left, and 6-mm-thick sensor on the right); reflected wavelength values are shown as a function of the indented points, for all the four FBGs. The optical fiber (thick yellow line), the FBG (thick blue line), and the indentation sites (black dots) are schematically represented at the bottom of the figure at hand. The reflected wavelength variations predicted by the model (blue line) are directly compared with the experimental data (red dots) each indentation site and each FBG, showing that the numerical simulations accurately predicted the experimental observation for both sensors.

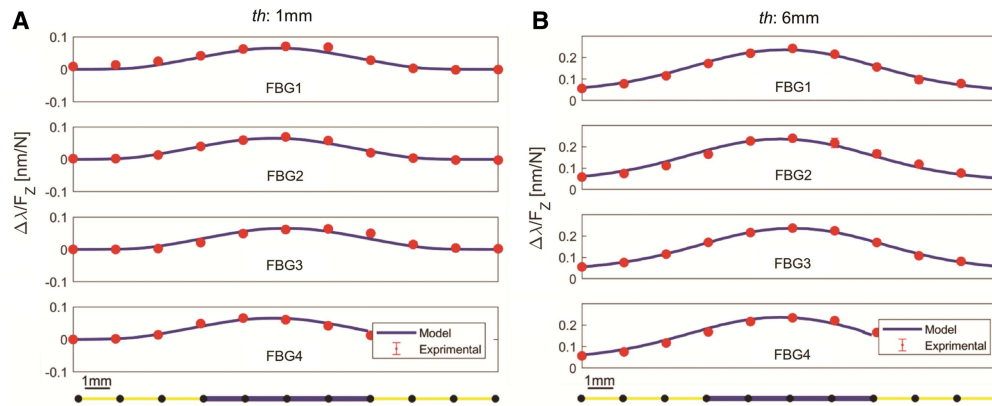


FIG. 8. Comparison of the experimental data (red dots) and the model data (blue line) for all the FBG sensors embedded in the soft polymeric matrix: **(A)** 1-mm-thick sensor; **(B)** 6-mm-thick sensor. The indented points (black dots) and the position of the FBG (blue line) are shown at the bottom of the figure. Color images are available online.

Sensor inverse function

The accuracies in sensing the indentation location by means of the proposed neural networks are reported in Figure 9. Training results, based on the numerical simulation data (for both the 1-mm-thick and the 6-mm-thick soft sensors), are shown in Figure 9A, while Figure 9B reports the validation results based on the experimental data. Each graph shows the estimated position, namely the output of the neural network, as a function of the nominal position, namely the target of the neural network. A perfect fit would correspond to a state where network output is equal to the targets (data on the bisecting solid line in figure). The correlation coefficient (R) and RMSE were calculated for each case. High R values ($R = 0.993$ for model training, $R = 0.992$ for validation, and $R = 0.991$ for experimental test) and low RMSE values (RMSE = 1.81 mm for model training, RMSE = 2.63 mm for validation, and RMSE = 2.45 mm for experimental test) were obtained when indenting the thicker sensor (for the thinner one, we got $R = 0.854$ and RMSE = 8.47 mm for model training, $R = 0.926$ and RMSE = 7.53 mm for validation, and $R = 0.844$ and RMSE = 10.73 mm for experimental test). The improved fitting of the thicker sensors was based on suitable cross talk among the FBGs. In the 1-mm-thick sensor, cross talk was negligible, especially between FBG2 and FBG3, and thus, the indentation location could not be accurately detected. The accuracy in sensing the indentation force is finally shown in Figure 10. We obtained the same trend as that one resulting when estimating the indentation position. High correlation and small error were obtained with the thicker sensor: $R = 0.998$ and RMSE = 0.029N for the model training, $R = 0.979$ and RMSE = 0.166 N for validation, and $R = 0.977$ and RMSE = 0.164 N for test (whereas for the thinner one, we obtained $R = 0.619$ and RMSE = 0.52 N for model training, $R = 0.307$ and RMSE = 0.58 for validation, and $R = 0.191$ and RMSE = 0.69 N for test). Table 1 summarizes the results of the adopted neural networks.

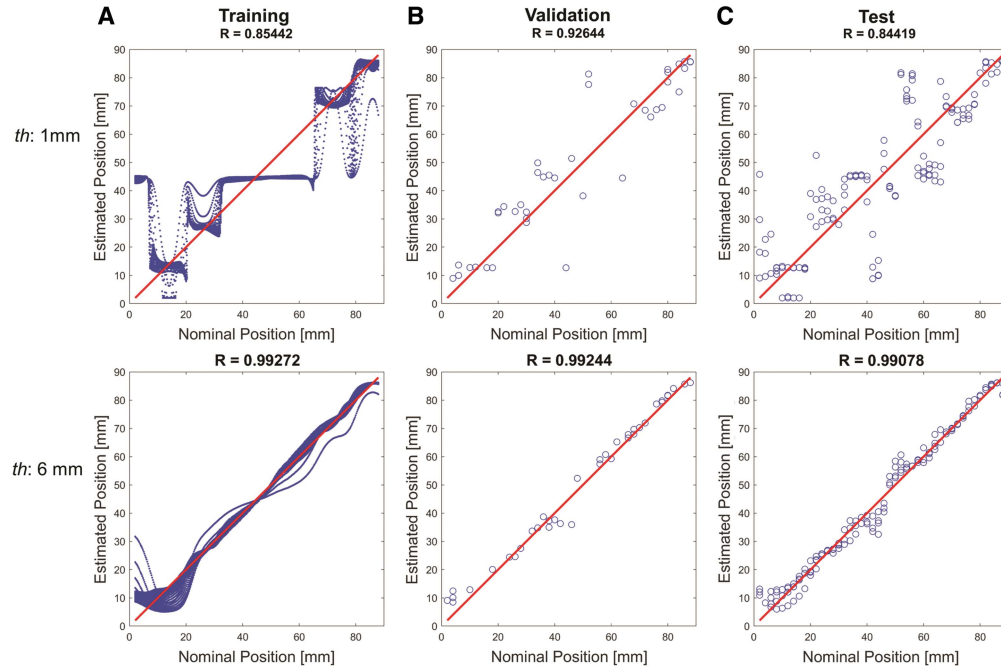


FIG. 9. Accuracy in sensing the indentation location by means of the proposed neural network, based on the developed numerical model, for both the 1-mm-thick and the 6-mm-thick sensors, Input: reflected wavelengths ($\lambda_1; \lambda_2; \lambda_3; \lambda_4$). Output: indenter location position along the optical fiber. **(A)** Training results. **(B)** Validation results. **(C)** Test results. Color images are available online.

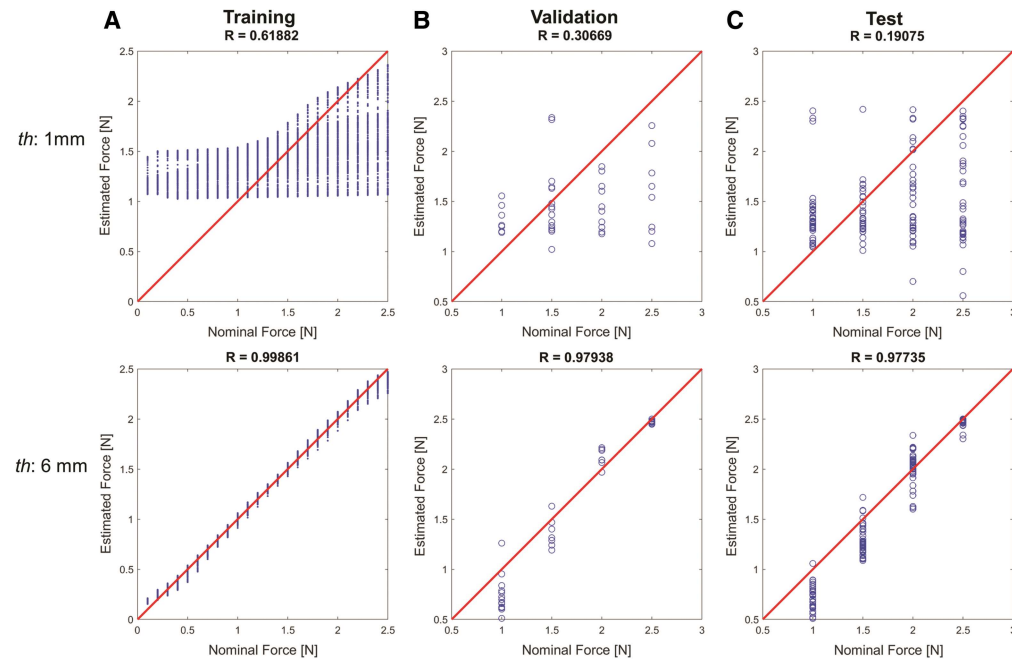


FIG. 10. Accuracy in sensing the force exerted by means of the proposed neural network, based on the developed numerical model, for both the 1-mm-thick and the 6-mm-thick sensors. Input: reflected wavelengths (λ_1 ; λ_2 ; λ_3 ; λ_4) and the probe position along the optical fiber. Output: force along the optical fiber. (A) Training results. (B) Validation results. (C) Test results. Color images are available online.

TABLE 1. CORRELATION COEFFICIENT AND ROOT MEAN SQUARE ERROR (Table view)

	<i>Model training NN1</i>	<i>Model training NN2</i>	<i>Experimental validation NN1</i>	<i>Experimental validation NN2</i>	<i>Experimental test NN1</i>	<i>Experimental test NN2</i>
<i>R</i> (1 mm)	0.85442	0.61882	0.92644	0.30669	0.84419	0.19075
RMSE (1 mm)	8.47 mm	0.52 N	7.53 mm	0.58 N	10.73 mm	0.69 N
<i>R</i> (6 mm)	0.99272	0.99861	0.99244	0.97938	0.99078	0.97735
RMSE (6 mm)	1.81 mm	0.029 N	2.63 mm	0.166 N	2.45 mm	0.164 N

NN1, first neural network; NN2, second neural network; *R*, correlation coefficient; RMSE, root mean square error.

Discussion and Conclusions

In this work, we presented the model-based development and calibration of a soft tactile sensor able to solve both the magnitude and the position of an applied normal load on its surface. Four FBG transducers housed in an optical fiber were embedded in a soft silicone brick. The silicone mediates the transmission of the applied load to the buried FBGs, thus inducing strain on the optical fiber, which in turns induces a shift of the nominal reflected wavelengths of the FBGs. Such a shift depends on both the applied load and the indentation site. We built a numerical model based on the working assumption of linear elastic sensor deformations in the range of forces considered, successfully validated through experimental results. We used the model to create a large calibration data set and machine learning to obtain the sensor inverse function.

As part of the numerical investigation, we considered a parametric sweep to probe the effect of sensor thickness on the receptive field of the gratings. Simulation results indicated that, for the chosen working parameters, a thickness of 6 mm contemporarily provided very good cross talk between sensors and proper sensitivity of individual sensors (whereas the 1-mm-thick cross talk between adjacent FBGs was much lower). Once calibrated the neural network with numerical results, it was able to resolve the applied normal load ($R = 0.97$) and its location ($R = 0.99$). In this study, we exploited the widely used neural networks available through a common software library: more refined algorithms could be used for achieving higher computational performances (even if the main computational burden with a neural network approach is associated with training, whereas the operation of the trained network is relatively lean). Moreover, since both the receptive field and the sensitivity of the buried FBGs are better in the thicker sensor, we provided evidence that the 6 mm sensor shows better performances in terms of localization and intensity prediction. Anyhow, in those applications where there are some constraints in terms of thickness or where flexibility is a key factor, the 1 mm sensor could be preferable compared with the 6 mm sensor.

With respect to previous studies, we originally demonstrated one main element of novelty: the capability to detect simultaneously, using machine learning and a numerical model of the sensor, the location and intensity of an applied load onto soft tactile sensors suitable for covering large areas in robotic applications. Nevertheless, we originally demonstrated a design/calibration methodology that can be extended to a wider set of materials and geometries, thus bringing a positive contribution at the crossroad between machine learning and soft tactile sensor design.

In this study, the sensor was calibrated by constraining its support during normal indentations distributed along its length. However, the proposed tactile sensor is intended to be wrapped, twisted, and attached on different surfaces. The minimum curvature radius allowed by the exploited fiber is 4 mm, to keep the strain below 1%; the maximum allowed axial strain is 5% (all these values are based on the datasheet). For our application (contact localization and contact force measurement), the aforementioned limits would put a constraint on the maximum curvature of the support upon which to lay on the polymeric matrix. For the specific sensor embodiment shown in this study, the maximum allowed twisting and bending angles were greater than $\pm 90^\circ$ and $\pm 180^\circ$, respectively, as shown in Supplementary Video S1. Such experimental conditions resulted in the following wavelength variations: $\Delta\lambda \approx 0.4$ nm for twisting, $\Delta\lambda \approx 1.5$ nm for bending, and $\Delta\lambda \approx 1$ nm for stretching. Moreover, it could be effectively used for a broad range of applications, including those where electromagnetic immunity is a key requirement (such as magnetic resonance imaging). Future works will address sensor design strategies and computational methods to decouple different sources of inputs in the sensor outputs. Scalability is another advantage of the proposed sensor. Indeed, multiple FBGs can be housed along the same optical fiber with only minor arrangements, thus enhancing sensing capabilities without penalizations in terms of bulkiness/complexity. Future studies will address dynamic effects and will involve the development of more complex geometries. As mentioned before, one of the main achievements of the present work is the model-based design and

calibration. Starting from such results, future works will involve the development of an artificial skin that aims at localizing the point of contact in a curved 2D matrix and the applied load force.

Author Disclosure Statement

No competing financial interests exist.

Funding Information

The study presented in this article was supported, in part, by the Italian Ministry of Education, Universities and Research within the “Smart Cities and Social Innovation Under 30” program through the PARLOMA Project (SIN_00132), in part, by the Dubai Future Foundation through Guaana.com open research platform, in part, by the Tuscany Region through the FAS Salute IMEROS Project, and, in part, by the Italian National Institute for Insurance against Accidents at Work through the SENSE-RISC Project.

Supplementary Material

Supplementary Figure S1

Supplementary Video S1

References

1. Johansson RS, Vallbo AB. Tactile sensibility in the human hand: relative and absolute densities of four types of mechanoreceptive units in glabrous skin. *J Physiol* 1979;286:283–300. Crossref. PubMed.
2. Johansson RS, Landstrom U, Lundstrom R. Responses of mechanoreceptive afferent units in the glabrous skin of the human hand to sinusoidal skin displacements. *Brain Res* 1982;244:17–25. Crossref. PubMed.
3. Johansson RS, Flanagan JR. Coding and use of tactile signals from the fingertips in object manipulation tasks. *Nat Rev Neurosci* 2009;10:345. Crossref. PubMed.
4. Oddo CM, Raspopovic S, Artoni F, et al. Intraneuronal stimulation elicits discrimination of textural features by artificial fingertip in intact and amputee humans. *Elife* 2016;5:e09148. Crossref. PubMed.
5. Dargahi J, Parameswaran M, Payandeh S. A micromachined piezoelectric tactile sensor for an endoscopic grasper-theory, fabrication and experiments. *J Microelectromech Syst* 2000;9:329–335. Crossref.
6. Wettels N, Santos VJ, Johansson RS, et al. Biomimetic tactile sensor array. *Adv Robot* 2008;22:829–849. Crossref.
7. Tiwana MI, Redmond SJ, Lovell NH. A review of tactile sensing technologies with applications in biomedical engineering. *Sens Actuators A Phys* 2012;179:17–31. Crossref.
8. Maness WL, Golden RF, Benjamin MH, et al. Pressure and contact sensor system for measuring dental occlusion. *US Patent* 4,856,993. August 15, 1989.
9. Puangmali P, Althoefer K, Seneviratne LD, et al. State-of-the-art in force and tactile sensing for minimally invasive surgery. *IEEE Sens J* 2008;8:371–381. Crossref.
10. Sorgini F, Mazzoni A, Massari L, et al. Encapsulation of piezoelectric transducers for sensory augmentation and substitution with wearable haptic devices. *Micromachines* 2017;8:270. Crossref.

11. Jacobus CJ, Riggs AJ, Taylor MJ. Method and system for providing a tactile virtual reality and manipulator defining an interface device therefor. *US Patent* 5,389,865. February 14, 1995.
12. Sorgini F, Massari L, D'Abbraccio J, et al. Neuromorphic vibrotactile stimulation of fingertips for encoding object stiffness in telepresence sensory substitution and augmentation applications. *Sensors* 2018;18:261. Crossref.
13. Caldwell DG, Tsagarakis N, Giesler C. An integrated tactile/shear feedback array for stimulation of finger mechanoreceptor. In: Proceedings 1999 IEEE International Conference on Robotics and Automation, 1999 (Cat. No.99CH36288C), Volume 1, Detroit, MI, May 10–15, 1999, pp. 287–292. IEEE.
14. Lee MH, Nicholls HR. Review Article Tactile sensing for mechatronics—a state of the art survey. *Mechatronics* 1999;9:1–31. Crossref.
15. Nicholls HR, Lee MH. A survey of robot tactile sensing technology. *Int J Rob Res* 1989;8:3–30. Crossref.
16. Dahiya RS, Metta G, Valle M, et al. Tactile sensing—from humans to humanoids. *IEEE Trans Robot* 2010;26:1–20. Crossref.
17. Harmon LD. Automated tactile sensing. *Int J Rob Res* 1982;1:3–32. Crossref.
18. Yousef H, Boukallel M, Althoefer K. Tactile sensing for dexterous in-hand manipulation in robotics—a review. *Sens Actuators A Phys* 2011;167:171–187. Crossref.
19. Tegin J, Wikander J. Tactile sensing in intelligent robotic manipulation—a review. *Ind Robot An Int J* 2005;32:64–70. Crossref.
20. Howe RD. Tactile sensing and control of robotic manipulation. *Adv Robot* 1993;8:245–261. Crossref.
21. Majidi C. Soft robotics: a perspective—current trends and prospects for the future. *Soft Robot* 2014;1:5–11. Crossref.
22. Trivedi D, Rahn CD, Kier WM, et al. Soft robotics: biological inspiration, state of the art, and future research. *Appl bionics Biomech* 2008;5:99–117. Crossref.
23. Kim S, Laschi C, Trimmer B. Soft robotics: a bioinspired evolution in robotics. *Trends Biotechnol* 2013;31:287–294. Crossref. PubMed.
24. Tolley MT, Shepherd RF, Mosadegh B, et al. A resilient, untethered soft robot. *Soft Robot* 2014;1:213–223. Crossref.
25. Ohmura Y, Kuniyoshi Y, Nagakubo A. Conformable and scalable tactile sensor skin for curved surfaces. In: Proceedings 2006 IEEE International Conference on Robotics and Automation, 2006, ICRA 2006, Orlando, FL, May 15–19, 2006, pp. 1348–1353. IEEE.
26. Hammond FL, Kramer RK, Wan Q, et al. Soft tactile sensor arrays for micromanipulation. In: 2012 IEEE/RSJ International Conference on Intelligent Robots and Systems (IROS), Vilamoura, Portugal, October 7–12, 2012, pp. 25–32. IEEE.
27. Kageyama R, Kagami S, Inaba M, et al. Development of soft and distributed tactile sensors and the application to a humanoid robot. In: IEEE SMC’99 Conference Proceedings. 1999 IEEE International Conference on Systems, Man, and Cybernetics, 1999, Volume 2, Tokyo, Japan, October 12–15, 1999, pp. 981–986. IEEE. Crossref.
28. Jamone L, Natale L, Metta G, et al. Highly sensitive soft tactile sensors for an anthropomorphic robotic hand. *IEEE Sens J* 2015;15:4226–4233. Crossref.
29. Kadowaki A, Yoshikai T, Hayashi M, et al. Development of soft sensor exterior embedded with multi-axis deformable tactile sensor system. In: The 18th IEEE International Symposium on Robot and Human Interactive Communication, 2009. RO-MAN 2009, Toyama, Japan, September 27–October 2, 2009, pp. 1093–1098. IEEE.
30. Tajima R, Kagami S, Inaba M, et al. Development of soft and distributed tactile sensors and the application to a humanoid robot. *Adv Robot* 2002;16:381–397. Crossref.
31. Wang X-D, Wolfbeis OS. Fiber-optic chemical sensors and biosensors (2008–2012). *Anal Chem* 2012;85:487–508. Crossref. PubMed.
32. Udd E, Spillman Jr WB. Fiber Optic Sensors: An Introduction for Engineers and Scientists. Hoboken, NJ: John Wiley & Sons, 2011. Crossref.
33. Polygerinos P, Zbyszewski D, Schaeffter T, et al. MRI-compatible fiber-optic force sensors for catheterization procedures. *IEEE Sens J* 2010;10:1598–1608. Crossref.
34. Barrias A, Casas JR, Villalba S. A review of distributed optical fiber sensors for civil engineering applications. *Sensors* 2016;16:748. Crossref.

35. Massaroni C, Saccomandi P, Schena E. Medical smart textiles based on fiber optic technology: an overview. *J Funct Biomater* 2015;6:204–221. Crossref. PubMed.
36. da Silva AF, Gonçalves AF, de Almeida Ferreira LA, et al. PVC smart sensing foil for advanced strain measurements. *IEEE Sens J* 2010;10:1149–1155. Crossref.
37. Silvestri S, Schena E. Optical-fiber measurement systems for medical applications. In: Predeep P. (Ed). Optoelectronics—Devices and Applications. London, UK: InTech, 2011, p. 4749.
38. Li H-N, Li D-S, Song G-B. Recent applications of fiber optic sensors to health monitoring in civil engineering. *Eng Struct* 2004;26:1647–1657. Crossref.
39. Ascari L, Corradi P, Beccai L, et al. A miniaturized and flexible optoelectronic sensing system for tactile skin. *J Micromech Microeng* 2007;17:2288. Crossref.
40. Heo J-S, Han C-H, Lee J-J. System design and evaluation of the robot tactile sensor using the microbending fiber optic sensors. In: The 16th IEEE International Symposium on Robot and Human Interactive Communication, 2007. RO-MAN 2007, Jeju, South Korea, August 26–29, 2007, pp. 14–18. IEEE.
41. Pirozzi S. Multi-point force sensor based on crossed optical fibers. *Sens Actuators A Phys* 2012;183:1–10. Crossref.
42. Liu X, Iordachita II, He X, et al. Miniature fiber-optic force sensor based on low-coherence Fabry-Pérot interferometry for vitreoretinal microsurgery. *Biomed Opt Express* 2012;3:1062–1076. Crossref. PubMed.
43. Liang Q, Zou K, Long J, et al. Multi-component FBG-based force sensing systems by comparison with other sensing technologies: a review. *IEEE Sens J* 2018;18:7345–7357. Crossref.
44. Li T, Shi C, Ren H. A high-sensitivity tactile sensor array based on fiber bragg grating sensing for tissue palpation in minimally invasive surgery. *IEEE/ASME Trans Mechatron* 2018;23:2306–2315. Crossref.
45. Saccomandi P, Oddo CM, Zollo L, et al. Feedforward neural network for force coding of an MRI-compatible tactile sensor array based on fiber Bragg grating. *J Sensors* 2015;2015:1–9. Crossref.
46. Song J, Jiang Q, Huang Y, et al. Research on pressure tactile sensing technology based on fiber Bragg grating array. *Photonic Sensors* 2015;5:263–272. Crossref.
47. Jiang Q, Xiang L. Design and experimental research on small-structures of tactile sensor array unit based on fiber Bragg grating. *IEEE Sens J* 2017;17:2048–2054. Crossref.
48. Negri LH, Paterno AS, Muller M, et al. Sparse force mapping system based on compressive sensing. *IEEE Trans Instrum Meas* 2017;66:830–836. Crossref.
49. Pedroso MA, Negri LH, Kamizi MA, et al. Fabrication of a tactile sensor array with fiber Bragg gratings using a 3D printed mold. In: 2017 SBMO/IEEE MTT-S International Microwave and Optoelectronics Conference (IMOC), Aguas de Lindoia, Brazil, August 27–30, 2017, pp. 1–4. IEEE.
50. Pedroso MA, Negri LH, Kamizi MA, et al. Tactile sensor array with fiber Bragg gratings in quasi-distributed sensing. *J Sensors* 2018;2018:1–8. Crossref.
51. Junjie B, Jianqing L, Ying W, et al. Composite tactile sensor array using fiber Bragg grating sensors and measuring system. In: 9th International Conference on Optical Communications and Networks (ICOON 2010), Nanjing, China, October 24–27, 2010. IET.
52. Heo J-S, Kim J-Y, Lee J-J. Tactile sensors using the distributed optical fiber sensors. In: 3rd International Conference on Sensing Technology, 2008. ICST 2008, Tainan, Taiwan, November 30–December 3, 2008, pp. 486–490. IEEE.
53. Massaroni C, Venanzi C, Silvatti AP, et al. Smart textile for respiratory monitoring and thoraco-abdominal motion pattern evaluation. *J Biophotonics* 2018;11:e201700263. Crossref. PubMed.
54. Ye X-W, Su Y-H, Xi P-S. Statistical analysis of stress signals from bridge monitoring by FBG system. *Sensors* 2018;18:491. Crossref.
55. Heo JS, Chung JH, Lee JJ. Tactile sensor arrays using fiber Bragg grating sensors. *Sens Actuators A Phys* 2006;126:312–327. Crossref.
56. Cutkosky MR, Howe RD, Provancher WR. *Force and tactile sensors*. In: Springer Handbook of Robotics. Berlin/Heidelberg, Germany: Springer, 2008, pp. 455–476. Crossref.

57. Ulmen J, Cutkosky M. A robust, low-cost and low-noise artificial skin for human-friendly robots. In: 2010 IEEE International Conference on Robotics and Automation (ICRA), Anchorage, AK, May 3–7, 2010, pp. 4836–4841. IEEE.
58. Heyneman B, Cutkosky MR. Biologically inspired tactile classification of object-hand and object-world interactions. In: 2012 IEEE International Conference on Robotics and Biomimetics (ROBIO), Guangzhou, China, December 11–14, 2012, pp. 167–173. IEEE.
59. Caldwell DG, Tsagarakis N, Wardle A. Mechano thermo and proprioceptor feedback for integrated haptic feedback. In: Proceedings, 1997 IEEE International Conference on Robotics and Automation, 1997, Volume 3, Albuquerque, NM, April 25, 1997, pp. 2491–2496. IEEE.
60. Jones LA, Lederman SJ. Human Hand Function. Oxford: Oxford University Press, 2006. Crossref.
61. Lun TLT, Wang K, Ho JDL, et al. Real-time surface shape sensing for soft and flexible structures using fiber Bragg gratings. *IEEE Robot Autom Lett* 2019;4:1454–1461. Crossref.
62. Cai L, Song L, Luan P, et al. Super-stretchable, transparent carbon nanotube-based capacitive strain sensors for human motion detection. *Sci Rep* 2013;3:3048. Crossref. PubMed.
63. Manuel CT, Harb R, Badran A, et al. Finite element model and validation of nasal tip deformation. *Ann Biomed Eng* 2017;45:829–838. Crossref. PubMed.
64. Hao Y, Gong Z, Xie Z, et al. A soft bionic gripper with variable effective length. *J Bionic Eng* 2018;15:220–235. Crossref.
65. Wang Z, Hirai S. Chamber dimension optimization of a bellow-type soft actuator for food material handling. In: 2018 IEEE International Conference on Soft Robotics (RoboSoft), Livorno, Italy, April 24–28, 2018. IEEE.
66. Zhang H, Kumar AS, Fuh JYH, et al. Topology optimized design, fabrication and evaluation of a multimaterial soft gripper. In: 2018 IEEE International Conference on Soft Robotics (RoboSoft), Livorno, Italy, April 24–28, 2018. IEEE. Crossref.
67. Mansy HA, Grahe JR, Sandler RH. Elastic properties of synthetic materials for soft tissue modeling. *Phys Med Biol* 2008;53:2115. Crossref. PubMed.
68. Feix T, Bullock IM, Dollar AM. Analysis of human grasping behavior: object characteristics and grasp type. *IEEE Trans Haptics* 2014;7:311–323. Crossref. PubMed.

Address correspondence to: Luca Massari, The BioRobotics Institute, Polo Sant'Anna Valdera, Scuola Superiore Sant'Anna, Viale Rinaldo Piaggio 34, Pontedera, Pisa 56025, Italy

E-mail: luca.massari@santannapisa.it

Edoardo Sinibaldi, Center for Micro-BioRobotics, Istituto Italiano di Tecnologia, Viale Rinaldo Piaggio 34, Pontedera, Pisa 56025, Italy

E-mail: edoardo.sinibaldi@iit.it

Calogero Maria Oddo, The BioRobotics Institute, Polo Sant'Anna Valdera, Scuola Superiore Sant'Anna,

Viale Rinaldo Piaggio 34, Pontedera, Pisa 56025, Italy

E-mail: calogero.oddo@santannapisa.it